journal

J. Am. Ceram. Soc., 94 [8] 2562–2570 (2011)
DOI: 10.1111/j.1551-2916.2011.04411.x

Thermal and Electrical Transport Properties of Spark Plasma-Sintered HfB_2 and ZrB_2 Ceramics

Luning Zhang, Dušan A. Pejaković, and Jochen Marschall*,†

Molecular Physics Laboratory, SRI International, Menlo Park, California 94025

Matthew Gasch*

Thermal Protection Materials and Systems Branch, NASA Ames Research Center, Moffett Field, California 94035

The thermal and electrical transport properties of various spark plasma-sintered HfB_2- and ZrB_2-based polycrystalline ceramics were investigated experimentally over the 298–700 K temperature range. Measurements of thermal diffusivity, electrical resistivity, and Hall coefficient are reported, as well as the derived properties of thermal conductivity, charge carrier density, and charge carrier mobility. Hall coefficients were negative confirming electrons as the dominant charge carrier, with carrier densities and mobilities in the $3–5 \times 10^{21}$ cm^{-3} and 100–250 $cm^2 \cdot (V \cdot s)^{-1}$ ranges, respectively. Electrical resistivities were lower, and temperature coefficients of resistivity higher, than those typically reported for HfB_2 and ZrB_2 materials manufactured by the conventional hot pressing. A Wiedemann–Franz analysis confirms the dominance of electronic contributions to heat transport. The thermal conductivity was found to decrease with increasing temperature for all materials. Results are discussed in terms of sample morphology and compared with data previously reported in the scientific literature.

I. Introduction

ULTRAHIGH TEMPERATURE CERAMIC (UHTC) composites based on HfB_2 and ZrB_2, together with minor silica-forming constituents such as SiC, Si_3N_4, $TaSi_2$, and $MoSi_2$, are under investigation for use in aerothermal heating environments as sharp leading edge components on future generations of hypersonic reentry vehicles.[1–3] Transition metal diborides have mechanical properties and brittle fracture behavior typical of ceramics, and yet their electrical and thermal conductivities are more characteristic of a metal.[4] The ability to effectively conduct heat is a desirable property for sharp leading edge components, as it improves their thermal shock resistance by reducing temperature gradients and thermal stresses within the material, and transports energy away from the stagnation point over a larger component surface area from which it can be efficiently radiated back to the environment.[5]

As typical of polycrystalline materials, the effective thermal and electrical conductivities of UHTC materials are affected by factors such as chemical composition, grain size, and porosity. The densification of pure ZrB_2 and HfB_2 materials by the conventional hot pressing of compound powders is difficult because of their hardness and very high melting points. Additives such as SiC, B_4C, and carbon can aid the sintering process; however, extreme conditions of pressure and temperature are generally required. Moreover, processing times can still reach hours, which encourages grain growth, undesirable from a mechanical property perspective. More recently, spark plasma sintering of elemental and compound powders, in which a pulsed DC current is applied during pressing, has been shown to produce dense ZrB_2 and HfB_2 composites at less extreme temperature and pressure conditions, and in shorter (tens of minutes) processing times.[6–8]

Here, we investigate the thermal and electrical transport properties of nine spark plasma-sintered (SPS) HfB_2- and ZrB_2-based polycrystalline ceramics over the 298–700 K temperature range. Thermal diffusivity, electrical resistivity, Hall effect measurements, and microscopy are performed on the same specimen of each ceramic. Thermal conductivity, charge carrier density, and charge carrier mobility are derived from the measured data. The measurement of both thermal and electrical properties allows the analysis of electron and phonon contributions to thermal transport.

II. Experimental Procedure

(1) Materials and Processing

Specimens from nine different UHTC billets were tested; seven billets were HfB_2-based materials and two were ZrB_2-based materials. We have grouped the nine samples into three characteristic groups. Group (A) consists of nominally pure diboride materials; group (B) consists of the composites prepared with excess elemental constituents: B1 (HfB_2–1% Ir), B2 (HfB_2–4% Hf or $HfB_{1.9}$), and B3 (HfB_2–2.5% B or $HfB_{2.1}$); group (C) consists of composites with SiC additions: C1 (HfB_2–5% SiC), C2 (HfB_2–5% SiC), and C3 (ZrB_2–20% SiC). Volume percentages are used throughout this paper. Sample labels, target compositions, and processing identifiers are summarized in the second and the third columns of Table I.

The diboride phase was produced from the reaction of elemental metal (Hf or Zr) and boron in all but two billets (C1 and C3), which were produced from milled diboride powders. The following raw powders were used: HfB_2 (−325 mesh, 99.5%, Cerac, Milwaukee, WI), ZrB_2 (−325 mesh, 99.5%, Cerac), Hf (−325 mesh, 99.8%, Cerac), Zr (−325 mesh, 99.7%, Cerac), B (amorphous, −325 mesh, 99%, Alpha Aesar, Ward Hill, MA), SiC (UF-05, 99.8%, H. C. Starck, Newton, MA), and Ir (−325 mesh, 99.95%, Surepure Chemetals, Florham Park, NJ).

All elemental powders were used as-purchased without additional milling. Powders were combined in desired proportions and hand mixed before pressing, either on the bench top or within a glove box to minimize humidity (processing method "dry#" in Table I). SiC powder was also used as-purchased when combined with elemental powders, as for specimen C2. For the billets made using diboride powders (processing method "/c-1" in Table I), the raw diboride and SiC powders were weighed and combined in the desired volumetric ratio, and then wet milled in cyclohexane with WC milling media in a planetary

R. Koc—contributing editor

Manuscript No. 28688. Received September 30, 2010; approved December 21, 2010.
This work was financially supported by the United States Air Force Office of Scientific Research, under contract FA9550-08-C-0049.
*Member, The American Ceramic Society.
†Author to whom correspondence should be addressed. e-mail: jochen.marschall@sri.com

Table I. Sample Groups, Target Volumetric Compositions, Processing Methods, Densities (Experimental, Theoretical, and their Ratio), Mean Intercept Length ($\bar{L} \pm \sigma$) from Log-Normal Fitting, and Grain-Boundary Area Per Unit Volume (S_V)

Group ID	Target composition	Processing ID	ρ_{exp} (g/cm^3)	ρ_{the} (g/cm^3)	ρ_{exp}/ρ_{the} (%)	$\bar{L} \pm \sigma$ (μm)	S_V (μm^{-1})
A1	HfB_2	TC1/—	11.0	11.21	98.1	10.7±4.9	0.205
A2	HfB_2	TC3/dry4	10.3	11.21	91.9	5.5±3.2	0.386
A3	ZrB_2	TC6/dry2	5.66	6.12	92.5	5.6±3.2	0.368
B1	HfB_2–1% Ir	TC5/—	11.1	11.33	98.0	10.3±4.2	0.200
B2	HfB_2–4% Hf[†]	TC7/dry1	11.0	11.29	98.1	10.0±5.1	0.218
B3	HfB_2–2.5% B[†]	TC8/dry1	11.1	10.99	101.0	10.9±5.8	0.191
C1	HfB_2–5% SiC	TC2/c-1	10.7	10.81	99.0	5.4±2.2	0.387
C2	HfB_2–5% SiC	TC4/dry1	11.0	10.81	101.8	5.5±3.3	0.415
C3	ZrB_2–20% SiC	TC9/c-1	5.50	5.54	99.3	A: 10.2±5.5 B: 3.9±1.9	AA: 0.215 AB: 0.206 Total: 0.421

[†]HfB_2–4% Hf = $HfB_{1.9}$ and HfB_2–2.5% B = $HfB_{2.1}$; A, ZrB_2; B, SiC.

mill (Fritsch Pulverisette 5, Fritsch, Idar-Oberstein, Germany). The milled powders were carefully dried to prevent phase segregation between the SiC and the denser diboride components.

All billets were consolidated by spark plasma sintering (Model SPS-1050, Sumitomo Heavy Industries Ltd., Tokyo, Japan) at the University of California Davis. Powders were packed into 20-mm-diameter graphite dies, loaded to 105–135 MPa, and densified at temperatures from 1700° to 1900°C, with hold times of 5–10 min. Heating rates during the SPS process were 100°–300°C/min. After pressing, test specimens were diamond-machined from the billets into 1-mm-thick, 12.7-mm-diameter disks. The thermal and electrical property measurements were performed on the same specimen from each billet.

(2) Sample Characterization

The densities of the test specimens were measured using the Archimedes method. The specimen crystal structure was characterized using an X-ray diffraction (XRD) apparatus (Phillips Electronics, New York, NY) with a Cu$K\alpha$ source and a Ge monochromator. After the completion of all thermal and electrical property testing, specimens were polished to a 1 μm finish (RotoPol-31, Struers, Willich, Germany), chemically etched with molten potassium hydroxide (99.99%, Alpha Aesar), and fractured into smaller specimens. The microstructure of both the etched and fractured specimen surfaces were characterized using a JEOL 6100 high-resolution field-emission scanning electron microscope (JEOL Ltd, Tokyo, Japan) with accompanying setup (EDAX, Mahwah, NJ) for elemental analysis by energy-dispersive spectroscopy (EDS).

Grain size analysis was performed on scanning electron microscope (SEM) images using the ImageJ program with the Concentric Circles plug-in.[9] Two circles of known radius were superimposed on each SEM image and the arc length crossing each grain was determined by measuring the central angle of the arc and converting it into an intercept length, L. This procedure is similar to those found in ASTM standard E 112-96.[10] Typically, 200–300 intercept length measurements were obtained for each etched specimen. From these measurements, an intercept length probability density histogram with 1 μm binning was constructed for each sample, and the histogram was fit by a log-normal distribution function

$$f(L) = \frac{1}{\sigma L\sqrt{2\pi}} \exp\left[-\frac{(\ln L - \mu)^2}{2\sigma^2}\right] \quad (1)$$

where the fitting parameters μ and σ are the mean and standard deviation of ln L. The mean and standard deviation of L are calculated from μ and σ by

$$\bar{L} = \exp\left(\mu + \frac{1}{2}\sigma^2\right) \quad (2)$$

$$\sigma_L = \exp\left(\mu + \frac{1}{2}\sigma^2\right)\sqrt{\exp(\sigma^2) - 1} \quad (3)$$

The mean grain size $\bar{D}$ is of similar magnitude to the mean intercept length $\bar{L}$, and various geometric approximations are available to make this conversion if desired.[11]

The grain-boundary interface area per volume, S_V, was also calculated for each specimen from the stereological relationship $S_V = 2N_{GB}/L_{tot}$, where N_{GB} is the total number of grain boundaries intersected by the two circles and L_{tot} is the sum of the two circle circumferences.[12]

(3) Thermal Diffusivity Measurements

Thermal diffusivity was measured using a photothermal radiometry technique in which the front face of a thin disk was periodically heated using a laser and the harmonic back-face temperature response was recorded and modeled to extract the thermal diffusivity. Photothermal techniques have been extensively developed and are widely used to measure the thermal properties of bulk and composite materials.[13–15] The experimental arrangement used in our measurements is shown in Fig. 1.

The UHTC specimen was mounted by its edge in a cylindrical aluminum holder fit with a band heater capable of heating specimens to about 450°C. Specimen temperature was measured by a type K thermocouple in direct contact with the specimen surface. A Synrad Firestar F400 CO_2 laser (output wavelength 10.6 μm), coupled to a Stanford Research Systems DG535 digital delay and pulse generator for output modulation, was used to irradiate the front face of the sample. A 3× beam expander (Haas Laser Technologies, Flanders, NJ) was used to expand the infrared beam diameter from about 3.5 mm at the laser exit to about 11 mm on the sample surface. This expansion made the

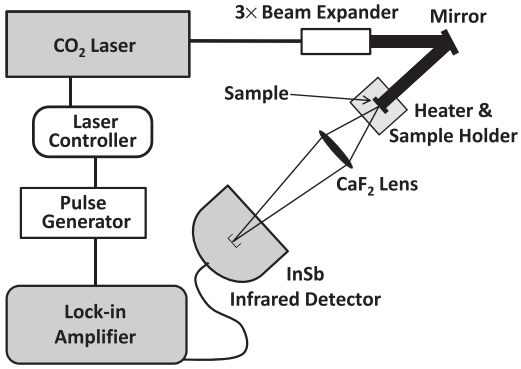

Fig. 1. Schematic of the photothermal radiometry setup for thermal diffusivity measurement.

Gaussian-like laser beam diameter much larger than the 1 mm sample thickness, assuring that heat transfer between the front and back faces of the sample was quasi one-dimensional near the center of the disk. Thermal emission originating from the center of the back face was focused by a CaF_2 lens onto a liquid nitrogen-cooled InSb detector (Model ND-2, Infrared Laboratories Inc., Tucson, AZ). The detector output voltage was processed by a Stanford Research Systems SR830 lock-in amplifier to extract its amplitude and phase shift as a function of laser modulation frequency. Because the amplitude of the harmonic temperature component, δT_b, was small ($\sim$0.1 K), the detected emissive power variations were essentially linearly proportional to δT_b, as can be verified from a blackbody radiation analysis.

A one-dimensional heat conduction model was used to determine the thermal diffusivity of the test specimens from the measured thermal emission. The harmonic component of the back-face temperature response to periodic front face heating is given by the complex expression[15]

$$\delta T_b = \frac{A}{\alpha} \frac{\exp(i\omega t)}{\sigma[\exp(\sigma d) - \exp(-\sigma d)]} \tag{4}$$

where α is the thermal diffusivity, d is the sample thickness, t is time, and $\omega = 2\pi f$ with f the laser heating frequency in Hz. In Eq. (4), $\sigma = [1+i]\sqrt{\omega/2\alpha}$ and the leading constant $A = I_0(1-R)/\rho c_p$, where I_0 is the laser intensity, R is the reflectance of the illuminated surface, ρ is the sample density, and c_p is the sample heat capacity. Through algebraic manipulation of Eq. (4), the magnitude and phase shift of the harmonic temperature response are, respectively,

$$|\delta T_b| = \frac{A}{\sqrt{2\alpha\omega\pi}} \left[\frac{1}{P^2(M-N)^2 + Q^2(M+N)^2} \right] \tag{5}$$

and

$$\Phi = \tan^{-1}\left[-\frac{P(M-N) + Q(M+N)}{D(M-N) - Q(M+N)} \right] \tag{6}$$

with $M = \exp(d\sqrt{\omega\pi/\alpha})$, $N = \exp(-d\sqrt{\omega\pi/\alpha})$, $P = \cos(d\sqrt{\omega\pi/\alpha})$, and $Q = \sin(d\sqrt{\omega\pi/\alpha})$.

Equations (5) and (6) can be used to derive the thermal diffusivity by fitting the measured magnitude and phase shift of the detected thermal emission as a function of laser modulation frequency. Use of Eq. (5) requires two fitting parameters, A and α, while Eq. (6) requires only α. In practice, we find phase shift fitting to be more reliable and reproducible than amplitude fitting because the amplitude of the harmonic temperature response becomes very small at high heating frequencies and is more susceptible to drifts in laser power and convective heat losses. Therefore, we report thermal diffusivity values derived by phase shift fitting. Based on the repeatability of measurements and fitting uncertainties, we estimate that reported thermal diffusivity values have uncertainties of about 5%. A standard graphite material, IG-110 nuclear grade from Toyo Tanso, Troutdale, OR, was used to verify the performance of our photothermal radiometry setup. Disk samples with thicknesses of 1 and 2 mm were used. The measured thermal diffusivity at about 299 K was 1.02 ± 0.03 cm^2/s, in very good agreement with the literature value of 1.03 cm^2/s at the same temperature.[16–17]

(4) Electrical Property Measurements

Figure 2 shows the experimental arrangements used for the electrical resistivity and the Hall coefficient measurements. Both measurements use a standard four-terminal van der Pauw geometry[18–19] in which current is driven between two terminals while voltage is measured between the remaining two terminals. A DC power supply (model 1302B, Global Specialties Instruments, Yorba Linda, CA) was used as a constant current source and a multimeter (model 2000, Keithley, Cleveland, OH) was used to measure voltages. Silver paint was used to form the electrical contacts between the silver lead wires and the disk samples. The Hall mobility measurements were performed in a custom-built electromagnet with a magnetic induction of 0.50 T (as measured using a Bell 600 Gaussmeter, F. W. Bell Inc., Orlando, FL). The electrical resistivity was measured as a function of temperature by placing the specimen on an electrically isolated heating stage. Sample temperatures were measured with a type K thermocouple.

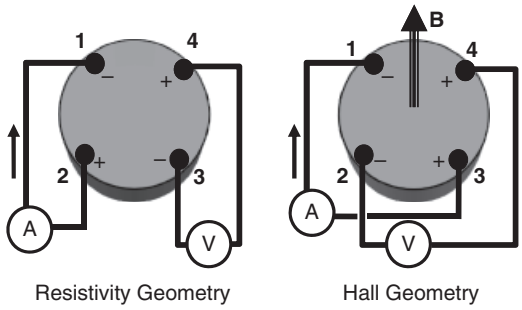

Fig. 2. Experimental geometries for electrical property measurements; the arrows indicate the direction of current flow for a particular test.

The sheet resistance for a van der Pauw measurement is $R_{ijkl} = V_{kl}/I_{ij}$, where the first two indices denote the positive (i) and negative (j) leads of the current input and the second two indices denote the positive (k) and negative (l) leads of the voltmeter. Figure 2 shows the van der Pauw geometry for measuring R_{2143}. In total, 24 measurements were made on each sample at each temperature. These consisted of three different current levels in the range of 1–2 A for each of the permutations $ijkl$ = 1234, 3412, 2143, 4321, 2341, 4123, 3214, and 1432. The three sheet resistances for each permutation were averaged and the electrical resistivity, r, was obtained by numerically solving the equation[18–19]

$$\exp\left(-\frac{\pi d(R_{1234} + R_{3412} + R_{2143} + R_{4321})}{4r}\right) + \exp\left(-\frac{\pi d(R_{2341} + R_{4123} + R_{3214} + R_{1432})}{4r}\right) = 1 \tag{7}$$

The performance of our setup was verified by making electrical resistivity measurements on thin sheets of nickel (0.125 mm, Aldrich, St. Louis, MO) and Constantan® (0.25 mm, Goodfellow, Oakdale, PA). Our measured room temperature resistivities for nickel (7.18 $\mu\Omega \cdot$cm) and Constantan® (50.4 $\mu\Omega \cdot$cm) are within a few percent of literature values.[20–21]

The Hall coefficient for a particular configuration is defined by $R^{\pm}_{H,ijkl} = V_{kl}d/I_{ij}B$, where the superscript (+ or −) defines the direction of the magnetic field perpendicular to the sample disk; the Hall geometry $R^{+}_{H,3142}$ is shown in Fig. 2. We fixed the current input and measured the voltage with the magnetic field turned off and on. In total, eight measurements were performed at a fixed current level (between 1 and 2 A) on each specimen: the permutations $ijkl$ = 1324, 3142, 2431, and 4213 for each of the two magnetic field directions (+0.5 and −0.5 T). The Hall coefficient was then computed as the average

$$R_H = (R^{+}_{1324} + R^{+}_{3142} + R^{+}_{2431} + R^{+}_{4213} + R^{-}_{1324} + R^{-}_{3142} + R^{-}_{2431} + R^{-}_{4213})/8 \tag{8}$$

The bulk carrier density and Hall mobility were computed as $n_e = 1/q_e R_H$ and $\mu_e = |R_H|/r$, respectively, where $q_e = -1.602 \times 10^{-19}$ C is the charge of an electron.

III. Experimental Results

(1) Microstructure and Composition

Theoretical densities were computed from the target volume fractions and the following pure component densities (in g/cm^3) $\rho_{HfB_2} = 11.212$,[4] $\rho_{ZrB_2} = 6.085$,[4] $\rho_{Hf} = 13.10$,[22] $\rho_B = 2.34$,[22] $\rho_{Ir} = 22.65$,[22] and $\rho_{SiC} = 3.214$.[23] The experimental and theoretical densities are listed in the fourth and the fifth columns of Table I. The experimental density values have estimated uncertainties of 1%. The sixth column of Table I shows that most specimens reached at least 98% of their theoretical density; the two exceptions are A2 (pure HfB_2) and A3 (pure ZrB_2), both of which are around 92% theoretical density. Two samples, B3 ($HfB_{2.1}$) and C2 (HfB_2–5% SiC) have densities higher than their theoretical values. The measured density of B3 is 1% higher than the theoretical value, suggesting that the final boron content did not reach the targeted 2.5% excess (or $HfB_{2.1}$ composition). The measured density of C2 is ~2% greater than the theoretical value, indicating that the actual SiC content is lower than the target 5% volume fraction.

The sample analysis by XRD shows the characteristic sharp diffraction peaks of crystalline ZrB_2 and HfB_2, as well as a variety of weaker peaks associated with impurities and minor constituents, as shown in Fig. 3. Diffraction peaks associated with HfO_2 are found for most HfB_2-based specimens. Diffraction peaks associated with HfC can be clearly identified for A2 (HfB_2), C1 (HfB_2–5% SiC), and C2 (HfB_2–5% SiC) and ZrC peaks can be identified for A3 (ZrB_2). No XRD peaks related to Ir (B1: HfB_2–1% Ir) or Hf (B2: HfB_2–5% Hf) were found. Diffraction peaks associated with SiC were observed for sample C3 (ZrB_2–20% SiC), but could not be clearly identified for samples C1 and C2 containing nominally 5% SiC.

Consistent with XRD results, SEM/EDS specimen characterization confirmed the presence of oxygen- and carbon-containing grains in most materials, and could not identify any Ir-containing grains or pure Hf grains in samples B1 and B2, respectively. A small population of boron particles was found in specimen C3 (ZrB_2–20% SiC), which was likely inadvertently introduced during the manufacturing process. SiC grains were sparse but clearly identifiable in sample C1. However, no SiC grains were found in sample C2. Instead, a variety of distinct HfC and carbon-rich grains were identified. This surprising finding is consistent with the presence of the strong HfC lines in the XRD spectrum (Fig. 3), as well as the aforementioned discrepancy between the measured density and theoretical density for this specimen. Specimen C2 was manufactured using elemental Hf and B powders, and the reaction $Hf + SiC \rightarrow Si + HfC$, which could lead to the loss of SiC, is thermodynamically favored.[24] However, EDS was unable to detect any Si-containing grains in sample C2.

Grain size analyses are presented in Fig. 4 as histograms with superimposed log-normal curve fits. The log-normal function provides a reasonable approximation to the experimental histograms. The values of $\bar{L}$ and σ_L derived from these fits are listed in Table I, along with the derived grain-boundary interface areas per unit volume. Values of $\bar{L}$ fall into two groups: one group around 5.5 μm and another around 10.5 μm. The samples with $\bar{L} \cong 5.5\,\mu m$ have roughly twice the grain-boundary interface area per volume than those with $\bar{L} \cong 10.5\,\mu m$. The grain composition was not considered during grain size analysis of samples C1 and C2. For sample C3, we have differentiated the two grain-boundary interfaces of ZrB_2–ZrB_2 and ZrB_2–SiC during analysis, and the individual and total interfacial areas of C3 are listed in Table I.

(2) Thermal Properties

The measured thermal diffusivities are plotted in Fig. 5 over the 298–700 K temperature range. The thermal diffusivity of all materials decreases with increasing temperature. The Ir-containing HfB_2 composite B1 has the highest thermal diffusivity and the pure HfB_2 material A2 has the lowest thermal diffusivity over this temperature range; this difference is about a factor of 1.5 at room temperature and 1.2 at 700 K.

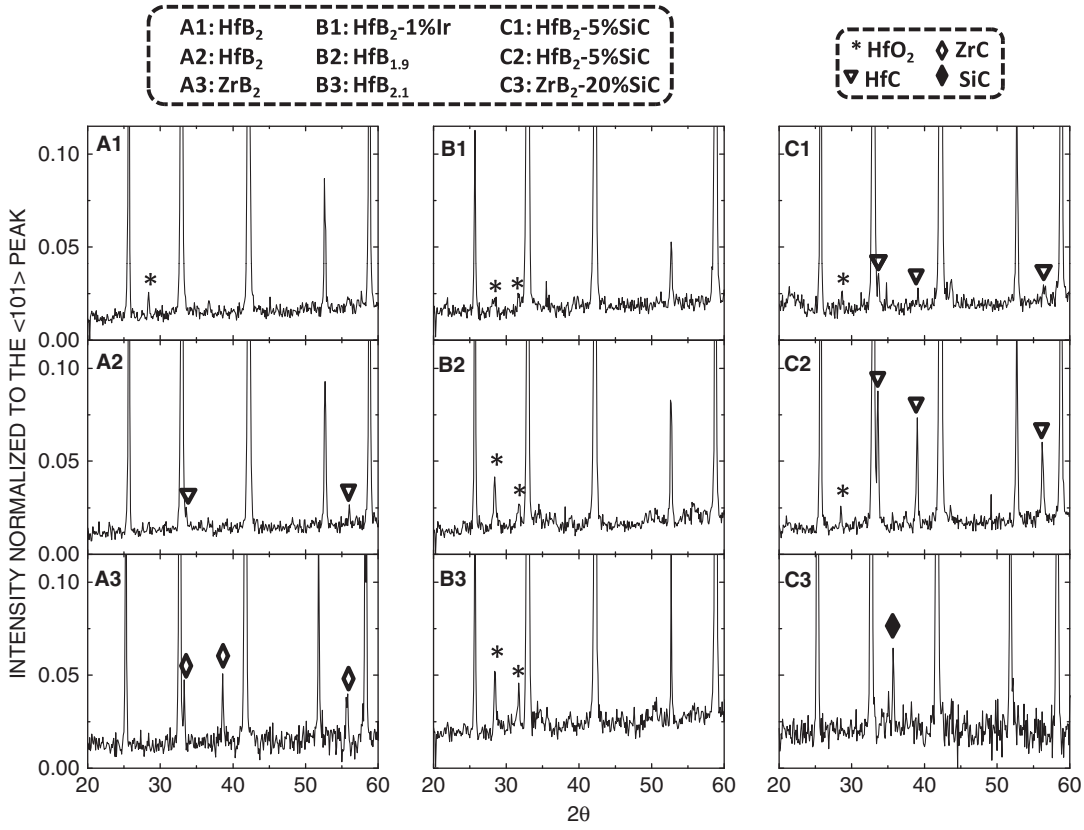

Fig. 3. X-ray diffraction scattering intensity versus scanning angle 2θ; intensities have been normalized to the <101> peak intensity.

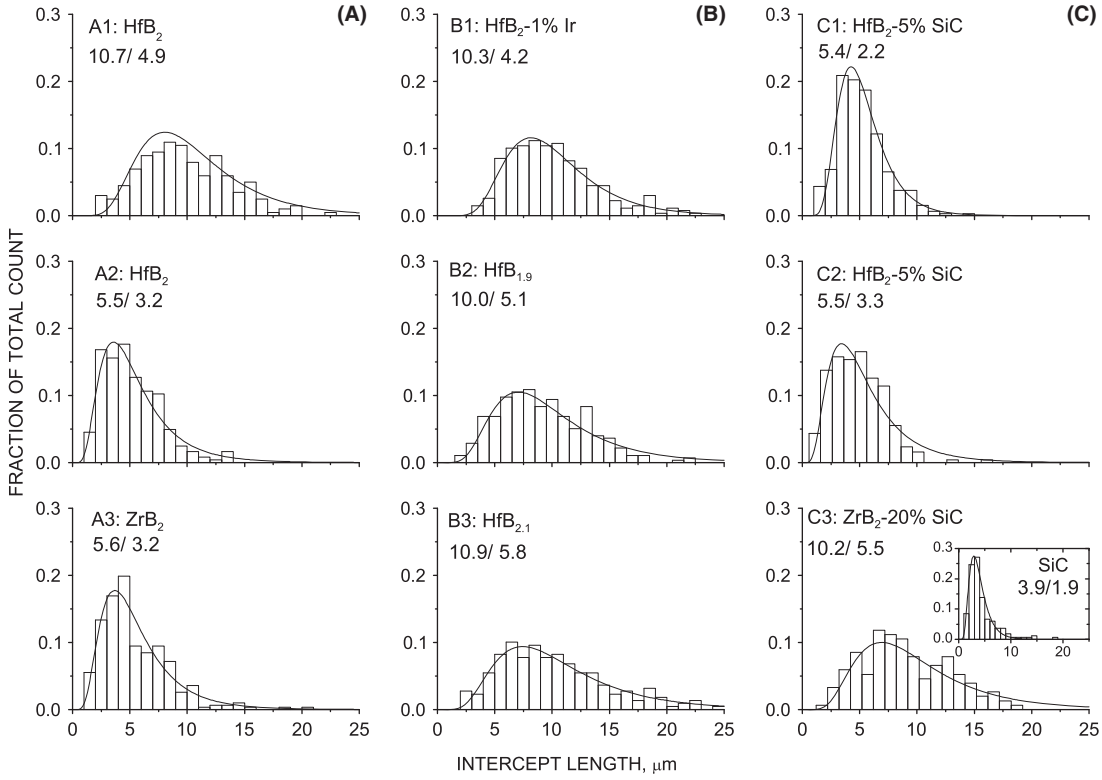

Fig. 4. Grain-size distributions obtained from the analysis of scanning electron microscopic images; the mean and standard deviations of the intercept lengths are indicated in each panel.

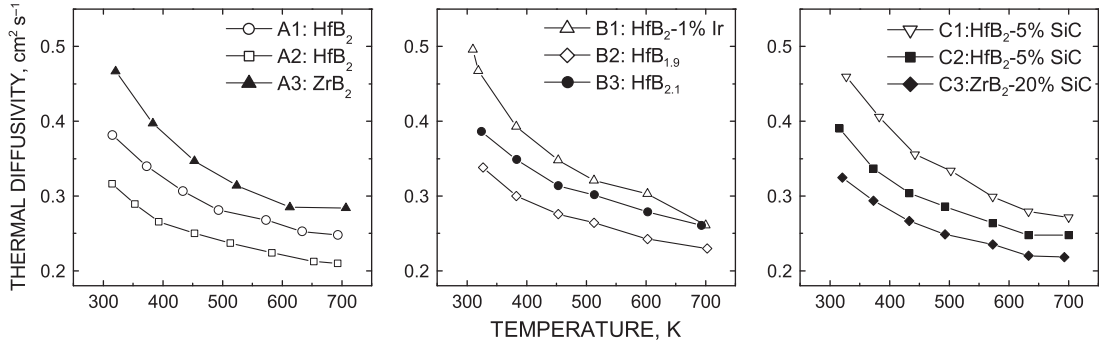

Fig. 5. Thermal diffusivities as a function of temperature.

Figure 6 shows thermal conductivity values computed from the measured thermal diffusivity data using the relation $\lambda = \alpha\rho c_p$. We have used the measured room-temperature densities of each sample, considering thermal expansion over the 298–700 K temperature range insignificant. Specific heat values for pure components were computed as a function of temperature using the expression

$$c_p(T) = A + BT + CT^{-2} + DT^2 \quad (9)$$

with coefficients derived from the HSC Chemistry database[24]; these coefficients are listed in Table II. For composite samples,

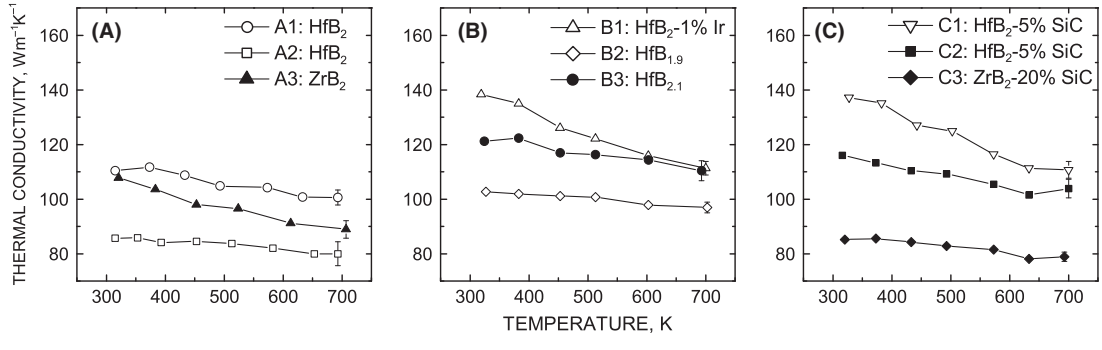

Fig. 6. Thermal conductivities calculated from the measured thermal diffusivities.

Table II. Specific Heat Function Parameters of Eq. (9)[24]

	A	B	C	D
HfB_2	366.52	0.03910	-1.150×10^7	0
ZrB_2 (<600 K)	−34.70	2.068	-4.830×10^5	-1.737×10^{-3}
ZrB_2 (>600 K)	583.45	0.06455	-1.417×10^7	5.131×10^{-6}
Hf	127.23	0.04645	2.527×10^5	1.681×10^{-9}
B	1483.16	1.193	-7.003×10^7	-2.992×10^{-4}
Ir	118.58	0.03218	2.091×10^5	-1.0×10^{-9}
SiC	824.55	0.5819	-2.786×10^7	-1.884×10^{-4}

specific heat values were mass-averaged using theoretical densities and nominal volume fractions. We estimate that the uncertainty in our computed specific heat values does not exceed 10%. The thermal conductivity of all materials also decreases over this temperature range, although not as strongly as the thermal diffusivity.

(3) Electrical Properties

Figure 7 shows the results of electrical resistivity measurements. Electrical resistivity increases linearly with increasing temperature for all samples. The data for each sample were fit by the equation

$$r = r_{298}[1 + \bar{\alpha}(T - 298)] \tag{10}$$

The resulting values of the room-temperature resistivity r_{298} and average temperature coefficient of resistivity, $\bar{\alpha}$, are listed in Table III. The values of r_{298} and $\bar{\alpha}$ for eight of the nine samples fall within the ranges 6–9 $\mu\Omega \cdot$cm and $3.5–4.3 \times 10^{-3}$ K^{-1}, respectively. The only exception is sample C3, which has a considerably higher room-temperature resistivity (17.0 $\mu\Omega \cdot$cm) and lower average temperature coefficient of resistivity (2.12×10^{-3} K^{-1}) than all the other samples because of its high SiC content. The electrical resistivity of SiC is very high compared with the diborides, on the order of 10 $\Omega \cdot$cm for undoped material.[25]

The final three columns of Table III list the measured Hall coefficient and the derived charge carrier density and Hall mobility for each sample. The measured Hall coefficients are all negative confirming that electron transport dominates charge flow in these materials. All Hall coefficients fall between -1.3×10^{-3} and -1.9×10^{-3} cm^3/C, with C2 having the lowest value and C3 the highest value. The carrier densities are in the range of $3.3–4.8 \times 10^{21}$ cm^{-3} and Hall mobilities in the range 100–220 $cm^2 \cdot (V \cdot s)^{-1}$. Samples A1 and C1 have the highest Hall mobility. Sample C2 has the highest carrier concentration, while C3 has the lowest values of both Hall mobility and carrier concentration.

(4) Electronic Contributions to Thermal Transport

The low electrical resistivity and the relatively high carrier density and Hall mobility of these diboride-based materials imply that electronic transport contributes substantially to heat transport. If the total thermal conductivity is taken as the sum of electronic and phonon contributions, $\lambda = \lambda_e + \lambda_{ph}$, and the electronic contribution is approximated by the Wiedmann–Franz relationship, it is possible to estimate the contribution of λ_e and λ_{ph} from the following:

$$\lambda_{ph}(T) = \lambda_{exp}(T) - \lambda_e(T) = \lambda_{exp}(T) - \frac{L_O T}{r_{298}[1 + \bar{\alpha}(T - 298)]} \tag{11}$$

The results of this estimation are shown in Fig. 8, where the ideal Lorenz Number, $L_O = 2.45 \times 10^{-8}$ $W \cdot (\Omega \cdot K^2)^{-1}$, is used. Table IV lists the room-temperature thermal and electrical

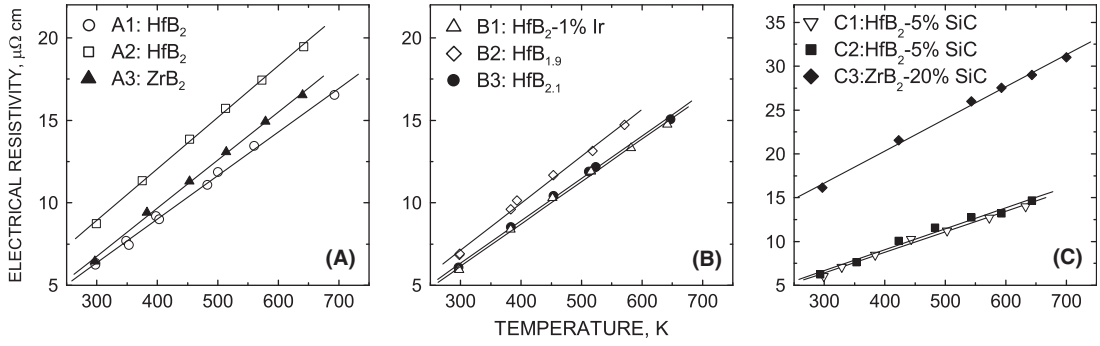

Fig. 7. Temperature dependence of the electrical resistivity; lines represent linear fits using Eq. (10).

Table III. Electrical Properties: Resistivity at 298 K (r_{298}), Temperature Coefficient of Resistivity ($\bar{\alpha}$), Hall Coefficient (R_H), Bulk Carrier Density (n_e), and Hall Mobility (μ_e)

Group ID	r_{298} ($\mu\Omega \cdot$cm)	$\bar{\alpha}$ ($\times 10^{-3}$ K^{-1})	R_H ($\times 10^{-3}$ cm^3/C)	n_e ($\times 10^{21}$ cm^{-3})	μ_e ($cm^2 \cdot (V \cdot s)^{-1}$)
A1	6.32	4.18	−1.60	3.9	220
A2	8.90	3.50	−1.64	3.8	170
A3	6.71	4.34	−1.55	4.0	200
B1	6.10	4.21	−1.76	3.5	250
B2	7.07	4.03	−1.63	3.8	200
B3	6.28	4.10	−1.46	4.3	210
C1	6.37	3.68	−1.55	4.0	220
C2	6.63	3.60	−1.30	4.8	180
C3	17.0	2.12	−1.89	3.3	100

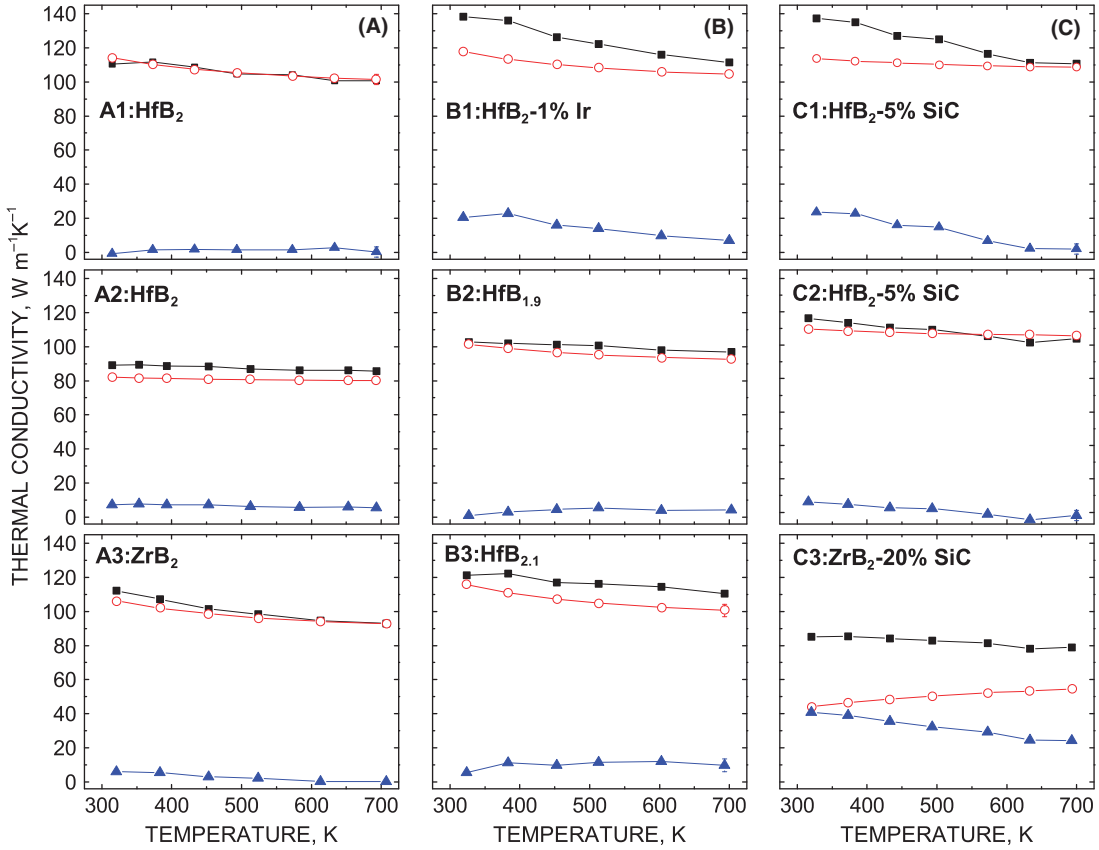

Fig. 8. Total (solid square), electronic (open circle), and phonon (solid triangle) thermal conductivities versus temperature; the electronic and phonon contributions are calculated from Eq. (11).

conductivities along with the room-temperature Wiedemann–Franz ratio ($\lambda_e/\lambda_{exp} = 298\sigma L_O/\lambda_{exp}$), which is higher than 0.8 for all materials except C3. Because Eq. (11) is based on a number of physical simplifications, and additionally propagates the experimental uncertainties associated with both our thermal and electrical property measurements, the absolute numerical values of $\lambda_{ph}(T)$ have a large uncertainty. Nevertheless, it is evident from Table IV and Fig. 8 that in 298–700 K temperature range, electronic contributions to the thermal conductivity dominate over phonon contributions.

IV. Discussion

The measured thermal conductivities are in the upper range of values reported for polycrystalline materials with similar composition, both pure diborides and their mixtures with SiC.[26–28] The effective (measured) thermal and electrical conductivities of polycrystalline ceramics depend on the individual constituent conductivities and the additional resistance to transport due to porosity and grain boundaries. Insight into these contributions can be gained through simple analytic models: the Brick Layer Model (BLM)[29] for interface resistance and the effective medium approximation (EMA)[30] for averaging constituent properties. The BML formula approximates the effect of interface resistance on thermal conductivity by

$$\lambda = \left(\frac{1}{\lambda_{int}} + \frac{R_\lambda}{a}\right)^{-1} \tag{12}$$

where R_λ is the thermal boundary resistance, a is the brick (grain) length, and λ_{int} is the intrinsic thermal conductivity. The EMA approach mixes constituent conductivities according to the implicit relationship

$$\sum_i v_i \frac{\lambda_i - \lambda_{eff}}{\lambda_i + 2\lambda_{eff}} = 0 \tag{13}$$

where v_i is the constituent volume fraction. Analogous equations apply for electrical conductivity.

For a composite in which porosity is isolated in a polycrystalline matrix of one major constituent, the two analytic models can be combined, with the BLM used to model the effect of grain-boundary resistance on the matrix conductivity and the EMA model used to incorporate the effect of porosity.[30–32] The "intrinsic" thermal and electrical conductivities of ZrB_2 and HfB_2 are not known, but based on the measurements of Kinoshita *et al.*[33] for single-crystal ZrB_2, reasonably representative values are $\lambda_{int} = 140\ W\cdot(m\cdot K)^{-1}$ and $\sigma_{int} = 2.17\times10^7$ S/m. With these values fixed, setting $a = \bar{L}$, and the porosity $\varepsilon = 1-\rho_{exp}/\rho_{the}$, the interfacial resistances can be adjusted until the computed effective conductivity matches the measured conductivity for the nominally pure diboride materials.

For the HfB_2 materials A1 and A2, the experimental room-temperature conductivities (Table IV) are matched with thermal interface resistances of 1.63×10^{-8} and $1.50\times10^{-8}\ m^2\cdot(K\cdot W)^{-1}$, and electrical interface resistances

Table IV. Values of Thermal Conductivity (Extrapolated), Electrical Conductivity, and the Wiedemann–Franz Ratio at 298 K

Group ID	λ_{298} ($W\cdot(m\cdot K)^{-1}$)	σ_{298} ($\times10^7$ S/m)	λ_e/λ_{exp}
A1	112	1.58	1.0
A2	89	1.12	0.92
A3	108	1.48	1.0
B1	138	1.62	0.86
B2	103	1.40	0.99
B3	125	1.58	0.92
C1	137	1.55	0.83
C2	118	1.50	0.93
C3	87	0.60	0.50

Table V. Published Electrical Property Measurements for HfB_2- and ZrB_2-Based Materials: Resistivity at 298 K (r_{298}), Temperature Coefficient of Resistivity ($\bar{\alpha}$), Hall Coefficient (R_H), Bulk Carrier Density (n_e), and Hall Mobility (μ_e)

Material	r_{298} ($\mu\Omega\cdot$cm)	$\bar{\alpha}$ ($\times 10^{-3}$ K^{-1})	R_H ($\times 10^{-3}$ cm^3/C)	n_e ($\times 10^{21}$ cm^{-3})†	μ_e (cm$^2\cdot$(V$\cdot$s)$^{-1}$)†	References
Polycrystalline						
HfB_2	15.8	—	−1.7	3.7	110	Juretschke and Steinitz[41]
HfB_2	16.6‡	—	−1.70	3.7	102	L'vov and Nemchenko[42]
HfB_2	10.4	3.29	−1.80	3.5	170	Samsonov *et al.*[43]
HfB_2–5% SiC	12.4	3.37	—	—	—	Tye and Clougherty[28]
ZrB_2	7	—	−2.0	3.1	290	Juretschke and Steinitz[41]
ZrB_2	16.6‡	—	−1.76	3.6	106	L'vov and Nemchenko[42]
ZrB_2	7.8	1.3	—	—	—	Rahman *et al.*[44]
ZrB_2	9.6	2.21	−1.90	3.3	200	Samsonov *et al.*[43]
ZrB_2	11.9	2.72	—	—	—	Tye and Clougherty[28]
ZrB_2 (90% dense)	11.0	3.73	—	—	—	Tye and Clougherty[28]
ZrB_2	22	2.06	—	—	—	Zimmermann *et al.*[27]
ZrB_2–20% SiC	10.3	4.42	—	—	—	Tye and Clougherty[28]
ZrB_2–30% SiC	24	2.52	—	—	—	Zimmermann *et al.*[27]
Single crystal						
ZrB_2	2.9–3.2‡	—	−1.2,§ −2.3¶	—	—	Piper[45]
ZrB_2	4.6‡	—	—	—	—	Kinoshita *et al.*[33]

†Computed from the tabulated r_{298} and R_H values assuming electrons are the charge carriers.
‡Room-temperature value, not from fitting.
§Parallel to hexagonal crystal axis.
¶Perpendicular to hexagonal crystal axis.

of 1.65×10^{-13} and 1.77×10^{-13} m^2/S, respectively. Because these interface resistances vary little between A1 and A2, the reduced thermal and electrical conductivities of A2 can be satisfactorily explained by its higher porosity and higher grain-boundary area per volume. A similar analysis of A3 gives lower thermal and electrical interface resistances of 0.60×10^{-8} m$^2\cdot$(K$\cdot$W)$^{-1}$ and 0.76×10^{-13} m$^2\cdot$S. The influence of grain-size distribution on effective conductivity can be incorporated into the BLM by setting $a=\bar{L}\exp(2.5(\sigma/\bar{L})^2)$.[34] The factor $\sigma/\bar{L}$ lies within the range 0.4–0.6 for all our materials; making this substitution for a increases the derived interface resistances by factors of 1.67, 2.32, and 2.25 for A1, A2, and A3, respectively. Typical thermal grain-boundary resistances in polycrystalline ceramics fall in the range 10^{-7}–10^{-9} m$^2\cdot$(K$\cdot$W)$^{-1}$ [29,35–36].

BLM/EMA analyses can also be performed for materials with additional constituents (e.g., Ir, SiC, excess Hf, excess B). Although "intrinsic" property inputs multiply, such modeling nevertheless suggests that the high thermal conductivities of C1 (HfB_2–5% SiC) and B1 (HfB_2–1% Ir) are better explained by lower thermal boundary resistances than as the result of high thermal conductivity second phases.

It is interesting to compare samples B2, A1, and B3, which were manufactured from elemental powders mixed to the stoichiometries $HfB_{1.9}$, HfB_2, and $HfB_{2.1}$, respectively. All three samples have similar grain sizes and grain-boundary area per volume. Sample B2 has the lowest thermal and electrical conductivities of the group, while B3 has a highest. However, enhanced electronic heat transport alone does not account for the entire difference in thermal conductivity between samples B2 and B3; the phonon contribution to thermal conductivity is also augmented in the higher boron content material (see Fig. 8 and Table IV). A similar observation can be made for samples C1 and B1; their high thermal conductivities seem to derive in part from additional phonon contributions to heat transport, not from enhanced electronic contributions (Fig. 8 and Table IV). The addition of minor constituents to diboride materials can exert a large influence on sintering behavior and chemistry at grain boundaries. We speculate that such additions, and the interface modifications they introduce, may influence the efficiency of electrical and phonon heat transport across grain boundaries in different ways.

Table V summarizes some published electrical property data for HfB_2- and ZrB_2-based materials. Similar to other investigators, we find high carrier mobilities for the diborides, with slightly lower Hall coefficients and slightly higher carrier densities for our SPS UHTC materials than typical in Table V. Our measured electrical resistivities are lower than most literature values for polycrystalline diborides manufactured by conventional hot-pressing methods. As shown in Fig. 8 and Table IV, a Wiedemann–Franz analysis for these SPS materials indicates that >80% of their total room-temperature thermal conductivity can be attributed to electronic contributions, except for sample C3 (ZrB_2–20% SiC) in which the contribution is 50%. Similar analyses presented in the literature vary widely. Zimmermann *et al.*[27] find electronic contributions of 50%–60% for ZrB_2 and ZrB_2–30% SiC; Samsonov *et al.*[37] report ~65% for ZrB_2 and HfB_2; Tye and Clougherty[28] derive contributions ranging from 40% to 90% for a variety of HfB_2 and ZrB_2 materials.

The Wiedemann–Franz relationship also predicts an increasing electronic contribution to thermal conductivity with increasing temperature if the temperature coefficient of resistivity is below $\bar{\alpha}<0.003356$ K^{-1} (i.e., <1/298 K; see Eq. (11)). We measure $\bar{\alpha}>0.003356$ K^{-1} for all our SPS samples except C3, whereas $\bar{\alpha}<0.003356$ K^{-1} for most materials in Table V. Both increasing ($d\lambda/dT>0$) and decreasing ($d\lambda/dT<0$) thermal conductivities with increasing temperature are reported in the literature for ZrB_2- and HfB_2-based materials.[26–27,37–40] We find $d\lambda/dT<0$ for all of our SPS UHTC materials. Researchers who have measured $d\lambda/dT>0$ and have also made temperature-dependent resistivity measurements report $\bar{\alpha}<0.003356$.[27,37] However, others have found $\bar{\alpha}<0.003356$ together with $d\lambda/dT<0$,[28] as in our data for sample C3. Because the phonon conductivity always decreases with increasing temperature, an additional mechanism is required to explain $d\lambda/dT>0$. Gasch *et al.*[26] have examined the closing of microcracks with increasing temperature as a possibility, but have found that an unsatisfactory explanation for various polycrystalline HfB_2 materials. It seems that $\bar{\alpha}<0.003356$ may be a necessary but insufficient condition for a diboride to exhibit increasing thermal conductivity with increasing temperature.

V. Conclusion

We investigated the thermal and electrical transport properties of SPS HfB_2- and ZrB_2-based polycrystalline ceramics with different microstructures and minor additives, in the 298–700 K temperature range. The materials have high carrier mobilities, with somewhat lower Hall coefficients and higher carrier densi-

ties than values typically reported for diboride-based polycrystalline materials. The measured electrical conductivities are higher than most literature values for diboride ceramics manufactured by conventional hot-pressing methods. The thermal conductivities are in the upper range of values typically reported for pure diboride and diboride–SiC compositions and all show decreasing conductivity with increasing temperature. A Wiedemann–Franz analysis indicates that thermal conductivity is dominated by the electronic contribution to thermal transport. The variations in thermal and electrical conductivities between different HfB_2 samples are explained by their different porosities and grain-boundary areas per volume. The high thermal conductivities of HfB_2–5% SiC and HfB_2–1% Ir samples are attributed to their low thermal boundary resistances. In samples of $HfB_{1.9}$, HfB_2, and $HfB_{2.1}$, which have very similar microstructures, both thermal and electrical conductivities increase with boron content, a finding that deserves further investigation.

Acknowledgment

The authors thank Prof. Zuhair Munir of the University of California at Davis for performing the SPS processing in support of this work.

References

[1]J. Fuller, Y. Blum, and J. Marschall, "Topical Issue on Ultra-High-Temperature Ceramics," *J. Am. Ceram. Soc.*, **91** [5] 1397–502 (2008).
[2]J. Fuller, G. Hilmas, W. Fahrenholtz, E. Corral, and L. Riegel, "Special Issue: Aerospace Materials for Extreme Environments," *J. Eur. Ceram. Soc.*, **30** [11] 2145–418 (2010).
[3]J. Fuller and M. Sacks, "Special Section: Ultra-High Temperature Ceramics," *J. Mater. Sci.*, **39** [19] 5885–6066 (2004).
[4]W. G. Fahrenholtz, G. E. Hilmas, I. G. Talmy, and J. A. Zaykoski, "Refractory Diborides of Zirconium and Hafnium," *J. Am. Ceram. Soc.*, **90** [5] 1347–64 (2007).
[5]T. H. Squire and J. Marschall, "Material Property Requirements for Analysis and Design of UHTC Components in Hypersonic Applications," *J. Eur. Ceram. Soc.*, **30** [11] 2239–51 (2010).
[6]U. Anselmi-Tamburini, Y. Kodera, M. Gasch, C. Unuvar, Z. A. Munir, M. Ohyanagi, and S. M. Johnson, "Synthesis and Characterization of Dense Ultra-High Temperature Thermal Protection Materials Produced by Field Activation through Spark Plasma Sintering (SPS): I. Hafnium Diboride," *J. Mater. Sci.*, **41**, 3097–104 (2006).
[7]S.-Q. Guo, T. Nishimura, Y. Kagawa, and J.-M. Yang, "Spark Plasma Sintering of Zirconium Diborides," *J. Am. Ceram. Soc.*, **91** [9] 2848–55 (2008).
[8]R. Licheri, R. Orrù, C. Musa, and G. Cao, "Combination of SHS and SPS Techniques for Fabrication of Fully Dense ZrB_2–ZrC–SiC Composites," *Mater. Lett.*, **62**, 432–5 (2008).
[9]W. S. Rasband, *ImageJ*. National Institutes of Health, Bethesda, MD, 2008.
[10]ASTM International. *Standard Test Methods for Determining Average Grain Size*. ASTM International, Materials Park, OH, 1996.
[11]J.-H. Han and D.-Y. Kim, "Analysis of the Proportionality Constant Correlating the Mean Intercept Length to the Average Grain Size," *Acta Metall. Mater.*, **43** [8] 3185–88 (1995).
[12]C. S. Smith and L. Guttman, "Measurement of Internal Boundaries in Three-Dimensional Structures by Random Sectioning," *Trans. Metall. Soc. AIME*, **197**, 81 (1953).
[13]D. P. Almond and P. M. Patel, *Photothermal Science and Techniques*. Chapman & Hall, New York, (1996).
[14]A. Salazar and A. Sánchez-Lavega, "Thermal Diffusivity Measurements Using Linear Relations from Photothermal Wave Experiments," *Rev. Sci. Instrum.*, **65** [9] 2896–900 (1994).
[15]A. Salazar, A. Sánchez-Lavega, and J. M. Terrón, "Effective Thermal Diffusivity of Layered Materials Measured by Modulated Photothermal Techniques," *J. Appl. Phys.*, **84** [6] 3031–41 (1998).
[16]M. Akoshima and T. Baba, "Thermal Diffusivity Measurements of Candidate Reference Materials by the Laser Flash Method," *Int. J. Thermophys.*, **26** [1] 151–63 (2005).
[17]M. Akoshima and T. Baba, "Study on a Thermal-Diffusivity Standard for Laser Flash Method Measurements," *Int. J. Thermophys.*, **27** [4] 1189–203 (2006).
[18]L. J. van der Pauw, "A Method of Measuring the Resistivity and Hall Coefficient of Lamellae of Arbitrary Shape," *Philips Tech. Rev.*, **20**, 220–4 1958/1959.
[19]L. J. van der Pauw, "A Method of Measuring Specific Resistivity and Hall Effect of Disks of Arbitrary Shape," *Philips Res. Rep.*, **13** [1] 1–9 (1958).
[20]B. Sundqvist, "Electrical Resistance of Nickel in the Range 300–725K and 0–2GPa," *Phys. Rev. B*, **38** [17] 12283–9 (1988).
[21]J. R. Davis, *ASM Specialty Handbook: Copper and Copper Alloys*. ASM International, Materials Park, OH, 2001.
[22]R. C. Weast, *CRC Handbook of Chemistry and Physics*, Vol. 60. CRS Press Inc., Boca Raton, FL, 1979-1980.
[23]R. G. Munro, "Material Properties of a Sintered α-SiC," *J. Phys. Chem. Ref. Data*, **26** [5] 1195–203 (1997).
[24]A. Roine, *HSC Chemistry for Windows, Version 5.11*. Outokumpu Research Oy, Pori, Finland, 2006.
[25]W. D. Kingery, H. K. Bowen, and D. R. Uhlmann, *Introduction to Ceramics*. John Wiley & Sons, New York, (1976).
[26]M. Gasch, S. Johnson, and J. Marschall, "Thermal Conductivity Characterization of Hafnium Diboride-Based Ultra High Temperature Ceramics," *J. Am. Ceram. Soc.*, **91** [5] 1423–32 (2008).
[27]J. W. Zimmermann, G. E. Hilmas, W. G. Fahrenholtz, R. B. Dinwiddie, W. D. Porter, and H. Wang, "Thermophysical Properties of ZrB_2 and ZrB_2–SiC Ceramics," *J. Am. Ceram. Soc.*, **91** [5] 1405–11 (2008).
[28]R. P. Tye and E. V. Clougherty, "The Thermal and Electrical Conductivities of Some Electrically Conducting Compounds"; pp. 396–401 in *Proceeding of the Fifth Symposium of Thermophysical Properties*, Edited by C. F. Bonilla, 1970.
[29]D. S. Smith, S. Fayette, S. Grandjean, and C. Martin, "Thermal Resistance of Grain Boundaries in Alumina Ceramics and Refractories," *J. Am. Ceram. Soc.*, **86** [1] 105–11 (2003).
[30]R. Landauer, "The Electrical Resistance of Binary Metallic Mixtures," *J. Appl. Phys.*, **23** [7] 779–84 (1952).
[31]C. Poulier, D. S. Smith, and J. Absi, "Thermal Conductivity of Pressed Powder Compacts: Tin Oxide and Alumina," *J. Eur. Ceram. Soc.*, **27**, 475–8 (2007).
[32]B. Nait-Ali, K. Haberko, H. Vesteghem, J. Absi, and D. S. Smith, "Thermal Conductivity of Highly Porous Zirconia," *J. Eur. Ceram. Soc.*, **26**, 3567–74 (2006).
[33]H. Kinoshita, S. Otani, S. Kamiyama, H. Amano, I. Akasaki, J. Suda, and H. Matsunami, "Zirconium Diboride (0001) as an Electrically Conductive Lattice-Matched Substrate for Gallium Nitride," *Jpn. J. Appl. Phys.*, **40** [12A] L1280–2 (2001).
[34]Z.-Y. Deng, J. M. F. Ferreira, Y. Tanaka, and Y. Isoda, "Microstructure and Thermal Conductivity of Porous ZrO_2 Ceramics," *Acta Mater.*, **55**, 3663–9 (2007).
[35]S. Fayette, D. S. Smith, A. Smith, and C. Martin, "Influence of Grain Size on the Thermal Conductivity of Tin Oxide Ceramics," *J. Eur. Ceram. Soc.*, **20**, 297–302 (2000).
[36]H.-S. Yang, G.-R. Bai, L. J. Thompson, and J. A. Eastman, "Interfacial Thermal Resistance in Nanocrystalline Yttria-Stabilized Zirconia," *Acta Mater.*, **50**, 2309–17 (2002).
[37]G. V. Samsonov, B. A. Kovenskaya, T. I. Serebryakova, and E. Y. Tel'nikov, "Thermal Conductivity of Diborides of Group IV–VI Transition Metals," *High Temp.*, **10** [6] 1193–5 (1972).
[38]M. M. Opeka, I. G. Talmy, E. J. Wuchina, J. A. Zaykoski, and S. J. Causey, "Mechanical, Thermal, and Oxidation Properties of Refractory Hafnium and Zirconium Compounds," *J. Eur. Ceram. Soc.*, **19**, 2405–14 (1999).
[39]M. Gasch, D. Ellerby, E. Irby, S. Beckman, M. Gusman, and S. Johnson, "Processing, Properties, and Arc Jet Oxidation of Hafnium Diboride/Silicon Carbide Ultra High Temperature Ceramics," *J. Mater. Sci.*, **39** [19] 5925–37 (2004).
[40]F. Monteverde and L. Scatteia, "Resistance to Thermal Shock and to Oxidation of Metal Diborides–SiC Ceramics for Aerospace Application," *J. Am. Ceram. Soc.*, **90** [4] 1130–38 (2007).
[41]H. J. Juretschke and R. Steinitz, "Hall Effect and Electrical Conductivity of Transition-Metal Diborides," *J. Phys. Chem. Solids*, **4** [1–2] 118–27 (1958).
[42]S. N. L'vov and V. F. Nemchenko, "Application of One-Band Concepts to the Diborides of Group IV Transition Metals," *Russ. Phys. J.*, **11** [1] 36–8 (1968).
[43]G. V. Samsonov, B. A. Kovenskaya, and T. I. Serebryakova, "Some Physical Characteristics of the Diborides of Transition Metals of Groups IV and V," *Russ. Phys. J.*, **14** [1] 11–4 (1971).
[44]M. Rahman, C. C. Wang, W. Chen, and S. A. Akbar, "Electrical Resistivity of Titanium Diboride and Zirconium Diboride," *J. Am. Ceram. Soc.*, **78**, 1380–2 (1995).
[45]J. Piper, "Galvanomagnetic Effects in Single-Crystal ZrB_2," *J. Phys. Chem. Solids*, **27**, 1907–15 (1966). □